The Interaction Between Deep Convection and Easterly Waves over Tropical North Africa: A Weather State Perspective

ADEME MEKONNEN AND WILLIAM B. ROSSOW

NOAA/Cooperative Remote Sensing of Science and Technology Center, The City College of New York, New York, New York

(Manuscript received 18 June 2010, in final form 10 January 2011)

ABSTRACT

The interaction between deep convection and easterly waves over tropical North Africa is studied using a weather state (WS) dataset from the International Cloud Climatology Project (ISCCP) and reanalysis products from the European Centre for Medium-Range Weather Forecast, as well as radiative fluxes from ISCCP and a precipitation dataset from the Global Precipitation Climatology Project. Composite analysis based on 21 yr of data shows that stronger latent and radiative heating of the atmosphere are associated with stronger, more organized, convective activity than with weaker, less organized, convective activity, implying that any transition from less to more organized and stronger convection increases atmospheric heating. Regression composites based on a meridional wind predictor reveal coherent westward propagation of WS and large-scale wind anomalies from the Arabian Sea into East Africa and through West Africa. The analysis shows that enhanced, but unorganized, convective activity, which develops over the Arabian Sea and western Indian Ocean, switches to organized convective activity prior to the appearance of the African easterly wave (AEW) signature. The results also suggest that low-level moisture flux convergence and the upper-tropospheric wind divergence facilitate this change. Thus, the upper-level easterly waves, propagating into East Africa from the Indian Ocean, enhance one form of convection, which interacts with the Ethiopian highlands to trigger another, more organized, form of convection that, in turn, initiates the low-level AEWs.

1. Introduction

African easterly waves (AEWs) are known to have an important influence on convection and rainfall on time scales less than 10 days over tropical West Africa (e.g., Carlson 1969a,b; Reed et al. 1977) and to be associated with tropical cyclone genesis over the tropical Atlantic (e.g., Avila and Pasch 1992). The mean structure and variability, including growth and propagation characteristics, of AEWs over West Africa (west of 10°E) are well studied, although not very well understood. We still lack a quantitative description of the relationship between various cloud types and weather systems and AEW phases. Relatively little is known about the AEW initiation, variability, and its association with convection over the source regions in East Africa. Thorncroft et al. (2008; hereafter referred to as THK08) provided a detailed review of two different (but not necessarily opposite) views in the literature concerning the origin and mechanisms of AEW initiation. To shed some light on these issues, we explore the role of deep convection in AEW initiation over East Africa and the mechanisms associated with convective variability relevant to AEWs during the boreal summer season (see Fig. 1 for orientation).

Earlier studies (e.g., Burpee 1972; Albignat and Reed 1980) viewed the initiation and growth of the AEWs as closely related to the presence of the middle-level African easterly jet (AEJ). In his pioneering work, Burpee (1972) found that the meridional gradient of the Ertel potential vorticity (PV) changes sign near 700 hPa over tropical North Africa and demonstrated that this PV gradient sign reversal satisfies the necessary condition for instability of an internal jet (Charney and Stern 1962). Consequently, Burpee (1972) concluded that AEWs grow on an unstable jet as a result of horizontal and vertical shear of the mean flow. Also, consistent with those studies, Norquist et al. (1977), based on observations, and Thorncroft and Hoskins (1994a,b), using an idealized modeling study, showed that AEWs grow because of mixed barotropic and baroclinic

Corresponding author address: Ademe Mekonnen, NOAA/CREST Center, T107 Steinman Hall, The City College of New York, CUNY, 140 St. and Convent Ave., New York, NY 10031.
E-mail: amekonnen@ccny.cuny.edu

DOI: 10.1175/2011JCLI3900.1

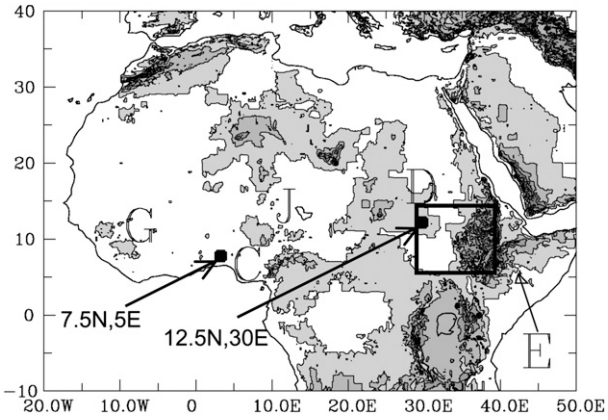

FIG. 1. Topographic map of tropical Africa. Contour interval is 500 m, and shading shows areas of elevation greater than 500 m above mean sea level. Highlands are designated by the following letters: E = Ethiopian highlands, D = Darfur mountains, C = Cameroon highlands, G = Guinea highlands, and J = Jos Mountains. The area delimited by the box (5°–15°N, 30°–40°E) defines the region area of interest. The heavy dots in West Africa (7.5°N, 5°E) and in East Africa (12.5°N, 30°E) show the location where baseline time series indices are constructed for use in the regression analysis (sections 2 and 4).

processes. Based on 2–5-day-filtered 850- and 700-hPa meridional wind variance, Albignat and Reed (1980) suggested that the AEWs form somewhere over the region west of 10°E and attain maximum amplitude over West Africa as they propagate westward in association with the AEJ. The basis for such a conclusion was that the wind variance amplitude over East Africa was weak compared with the amplitude over West Africa. However, weak wave activity over East Africa is not inconsistent with the presence of AEWs there if they are at their initial stages of development (e.g., Mekonnen et al. 2006, hereafter referred to as MTA06; Kiladis et al. 2006, hereafter referred to as KTH06).

In contrast, based on a synoptic case study in the summer of 1968, Carlson (1969a,b) suggested that the source region of AEWs is in eastern Africa and that these waves are initiated in association with convection over the mountains in Sudan and Ethiopia. Recent research, both modeling and observational, supports Carlson's suggestion. MTA06 showed that AEWs are initiated in association with convective activity over the Darfur Mountains in the Sudan and, occasionally, upstream from the Ethiopian highlands. KTH06 provided evidence that the AEW-related convection that attains maximum amplitude over West Africa is first seen as a weak convective signature over central Sudan. Based on another synoptic case study, Berry and Thorncroft (2005) argued that the AEWs form as a dynamic response to a large region of convective activity composed of mesoscale systems near the Darfur region. Also, Lin et al. (2005) showed that the AEW that was associated with the formation of Hurricane Alberto in 2000 had its origin from mesoscale convective activity over the Ethiopian highlands. Modeling studies by Hall et al. (2006; hereafter referred to as HKT06) and THK08 have shown that the AEWs are, indeed, forced by a finite-amplitude precursor in East Africa and that the midlevel AEJ is only marginally unstable. THK08 highlighted that the convective triggers are location sensitive and suggested that a convective outburst in the Darfur region favors AEW initiation (see also Leroux and Hall 2009). A recent study on the interaction between intraseasonal variability and synoptic scale activity over tropical Africa by Leroux et al. (2009) also suggests that increased synoptic-scale activity over West Africa is related to enhanced convection on an intraseasonal time scale but also follows active convection over the East. Similarly, in a modeling study, Hsieh and Cook (2005) proposed that the presence of the AEJ is not a necessary condition for the AEWs; instead, they pointed out the impact of moist convection on the basic state that supports the initiation of AEWs.

Most of our understanding about the relationship between AEWs and convection is based on observations and analyses over West Africa, where AEWs attain their maximum amplitude. Work that incorporates the circulation features and mechanisms that determine synoptic-scale variability of convection over eastern Africa and the associated initiation of AEWs is less developed. This is due to a combination of factors including scarcity of observational data over the region. Moreover, our knowledge of the climate of East Africa is very limited (see also Washington et al. 2006 for detailed review on our knowledge and understanding of climate over sub-Saharan Africa). A recent body of work (e.g., MTA06; THK08; HKT06) has emphasized the importance of East African convection to the AEWs initiation.

We revisit the issue of AEW genesis by exploring the nature of convective activity and its relationship with AEWs over East Africa. We take a different approach from previous studies by utilizing 21 years of daily data characterizing the large-scale atmospheric state and moisture, together with the characteristics of convection from satellite observations. In particular we use the weather state (WS) dataset that was introduced by Jakob and Tselioudis (2003) and Rossow et al. (2005; hereafter referred to as RTPJ). Conventional satellite studies using only infrared brightness temperature anomalies give us a rough estimate of the location and propagation of convection associated with wave disturbances, but, as we show, this approach mixes together distinctly different conditions. The weather state data, together with other observations of precipitation, radiation, and atmospheric state, provide much more information and a clearer picture of the different types of tropical convection and their association

with wave disturbances. We will show a specific sequence of events, involving propagating waves and distinct convective transitions, that occurs near the Ethiopian highlands and triggers AEWs downstream of the highlands.

After a brief overview of the various datasets used and the analysis methodology employed in section 2, we briefly review in section 3 the tropical North African climatology with an emphasis on the eastern part to provide context. Section 4 discusses the results of our analysis of the relationship of different types of deep convection and AEWs. The mechanisms that are associated with convective organization over East Africa are also investigated in this section. A summary of major findings and final remarks are given in section 5.

2. Data and analysis methodology

a. Data

Previous observational studies of AEW and convection have used satellite-observed infrared brightness temperatures [sometimes referred to as outgoing longwave (LW) radiation (OLR)] as a proxy for deep convective activity and kinematic indices based on, for example, the 850- and 700-hPa winds (Burpee 1972; KTH06; MTA06; Pytharoulis and Thorncroft 1999). Here, we use the International Satellite Cloud Climatology Project (ISCCP) weather state and European Center for Medium-Range Weather Forecasts (ECMWF) reanalysis temperature, humidity, and winds datasets.

1) WEATHER STATE DATA FROM ISCCP

Tropical WSs are identified by distinct mesoscale patterns in the horizontal distribution of cloud properties based on the ISCCP (Schiffer and Rossow 1983; Rossow and Schiffer 1999). The ISCCP D1 data provide the joint frequency distributions of cloud-top pressure (CTP) and optical thickness (τ) from individual satellite image pixels (field of view about 5 km) occurring within each 2.5° horizontal map grid (a scale of about 300 km) at 3-h time intervals during the daytime. As described in Jakob and Tselioudis (2003) and RTPJ, tropical cloud regimes can be defined objectively by distinctive patterns in these joint frequency distributions using, for example, the K-means cluster analysis method (Anderberg 1973). RTPJ's analysis of the whole tropics (15°S–15°N) found six WSs.[1] Following the procedures described in RTPJ, we extended the analysis to a domain including the subtropics (35°S–35°N) over the period July 1983–December 2004 (Fig. 2; same period of record as in RTPJ). Two additional marine boundary layer weather state types appear in the expanded zone. This dataset is available at the Cooperative Remote Sensing Science and Technology Center at the City College of New York. (Additional information can be found at http://www.crest.ccny.cuny.edu/rscg/index.html. Also, the basic definition of ISCCP cloud types including cloud classification with respect to CTP–τ can be found online at the Goddard Institute for Space Studies of the National Aeronautics and Space Administration, http://isccp.giss.nasa.gov/cloudtypes.html.) More details about the weather state dataset can also be found in RTPJ.

Figure 2 presents the eight patterns of the joint histograms of CTP–τ, called WSs, which describe variations of cloud properties for the whole region 35°S–35°N. The relative frequency of occurrence (RFO) for each WS over the whole domain is given at the top-right corner of each plot. The presence of clouds with the largest τ and smallest CTP is indicative of deep convective clouds (cf. Fu et al. 1990; Machado and Rossow 1993; Machado et al. 1998). Weather states 1, 2, and 3 (WS1, WS2, and WS3, respectively) in the top panels have some clouds with larger τ and low CTP and are, hence, referred to as convectively active states. As described by RTPJ, WS1 (RFO = 5.9%) is the most convectively active cloud regime (more deep convective clouds—more area covered—as indicated by the color scale in Fig. 2) and is associated with larger mesoscale systems (MCSs) that also include thick cirrostratus anvil clouds. WS2 (RFO = 8.5%) has less deep convection and more cirrostratus clouds but is generally closely associated with WS1 in space and time. WS3 (RFO = 17.4%) has more clouds with lower cloud tops and lower τ (compared with WS1, WS2) but still has some large τ–low CTP clouds (in the upper right) indicating isolated, smaller-scale convective systems. RTPJ also noted that WS2 and especially WS3 include the cumulus congestus as indicated by clouds with midlevel tops and large optical thicknesses. WS3 occurs more frequently than WS1 or WS2. As shown by Machado and Rossow (1993; their Fig. 8), the area ratio of convective to anvil clouds in tropical convective system is roughly constant; hence, the larger convective cloud amount in WS1 and the smaller amount in WS3 is associated with larger and smaller convective systems. Moreover, the fraction of total area covered by each size range is roughly the same, so that the less frequent WS1 (5.9%) occupies about the same area of the region (35°S–35°N) as the more frequent WS3 (17.4%).

WS4 (RFO = 9.6%) and other weather states represent convectively suppressed states with different types of boundary layer clouds and cirrus (especially WS4). WS4 is mainly thin cirrus (top-left corner). Since weather states 5–8 (WS5678) represent shallow boundary layer

[1] In this method the completely clear condition is treated as a separate category; it is very rare in the tropics.

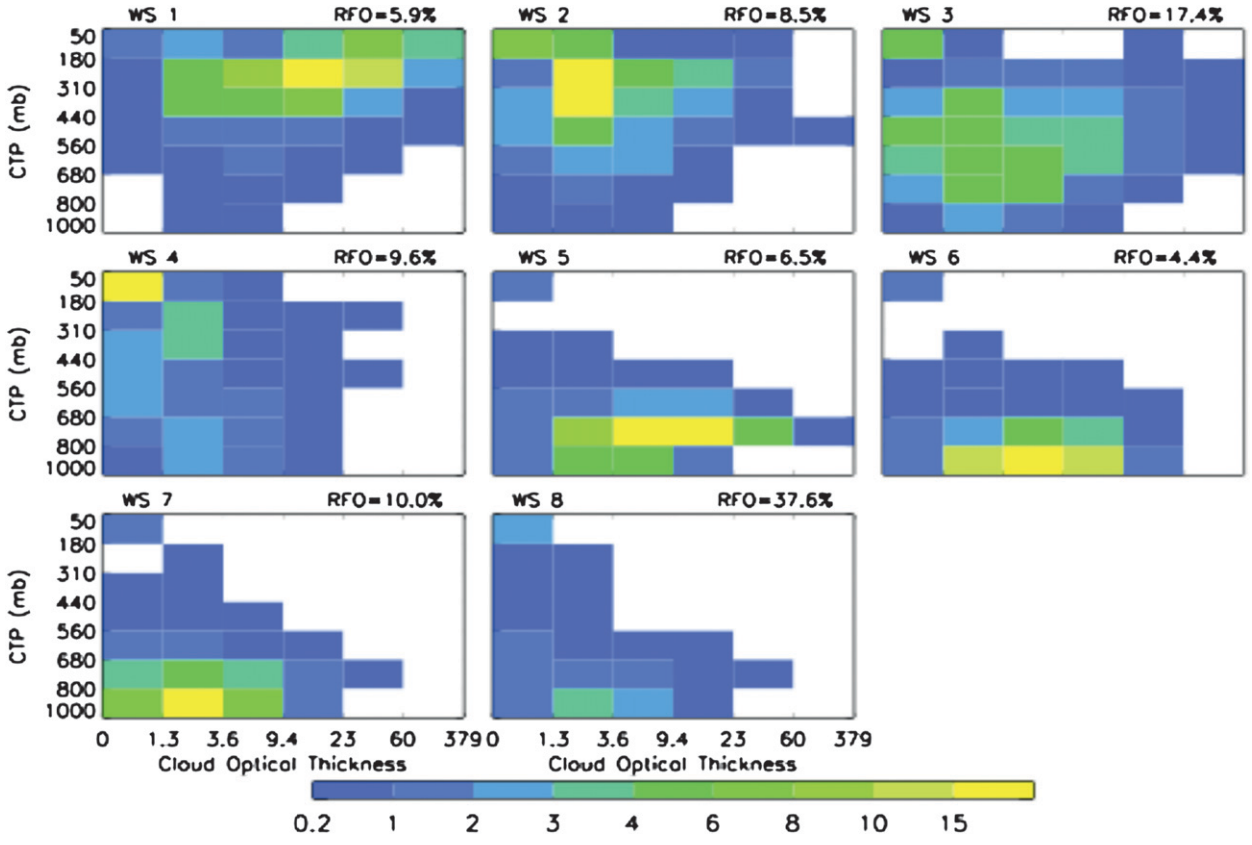

FIG. 2. The frequency of occurrences of cloud-top pressure–optical thickness patterns, called WSs. The histogram is averaged for global subtropics in ±35° and for 7/1983–12/2004 based on ISCCP D1 data. The WS are numbered from 1 to 8 and are described from (top) most convectively active to (middle, bottom) least convectively active (cf. RTPJ). The WS RFO (in percent of domain) are shown on the top-right corner of each plot.

clouds mainly located over subtropical ocean regions in the vicinity of seasonal high-pressure areas, we aggregate them in subsequent displays.

Figure 3 shows the global distribution of WS1 through WS4 and WS5678 for the July–September (JAS) season (averaged over 1984–2004; the percentages shown are with respect to the total WS types). WS1 is most frequently seen over the high terrain in Cameroon–Nigeria and Guinea. WS2 is most frequent over central Africa. WS3 is most frequent over the highlands in Ethiopia, Cameroon–Nigeria, and Guinea. The convectively active cloud regimes are collocated over the summertime intertropical convergence zone (ITCZ) and peak summertime rainfall belt (cf. Fig. 4), indicating their association with the seasonal upward motion. WS4—representing high cirrus, some related to the outflow from convective systems—is widespread over the African portion of the ITCZ. The rest of the convectively inactive regimes represented by WS5678 are concentrated in the subtropical regions over land and in the vicinity of oceanic seasonal high pressure areas and are least frequent within the ITCZ area.

2) ECMWF REANALYSIS

The large-scale atmospheric state and dynamics are obtained from the 40-yr ECMWF Re-Analysis (ERA-40) product. ERA-40 describes the state of the atmosphere at 6-hourly intervals in a 2.5° horizontal grid with 23 pressure levels. The observational data that went into the reanalysis are sparse over Africa, especially over the eastern part, except for the satellite-based information. However, the performance of ECMWF reanalysis for synoptic-scale study of AEWs was tested by Reed et al. (1988) and was found to be satisfactory. As will be shown later, the analysis based on ISCCP WS and ERA-40 reveals coherent structures that give us confidence in the results from dynamical fields. ERA-40 is available from September 1957 to August 2002. Here, we use daily averages from 1984–2001.

3) GPCP RAINFALL AND ISCCP RADIATIVE FLUX DATASETS

We use the one degree daily version 1.1 (1DD V1.1) version of the Global Precipitation Climatology Project (GPCP) products that provide values at daily intervals

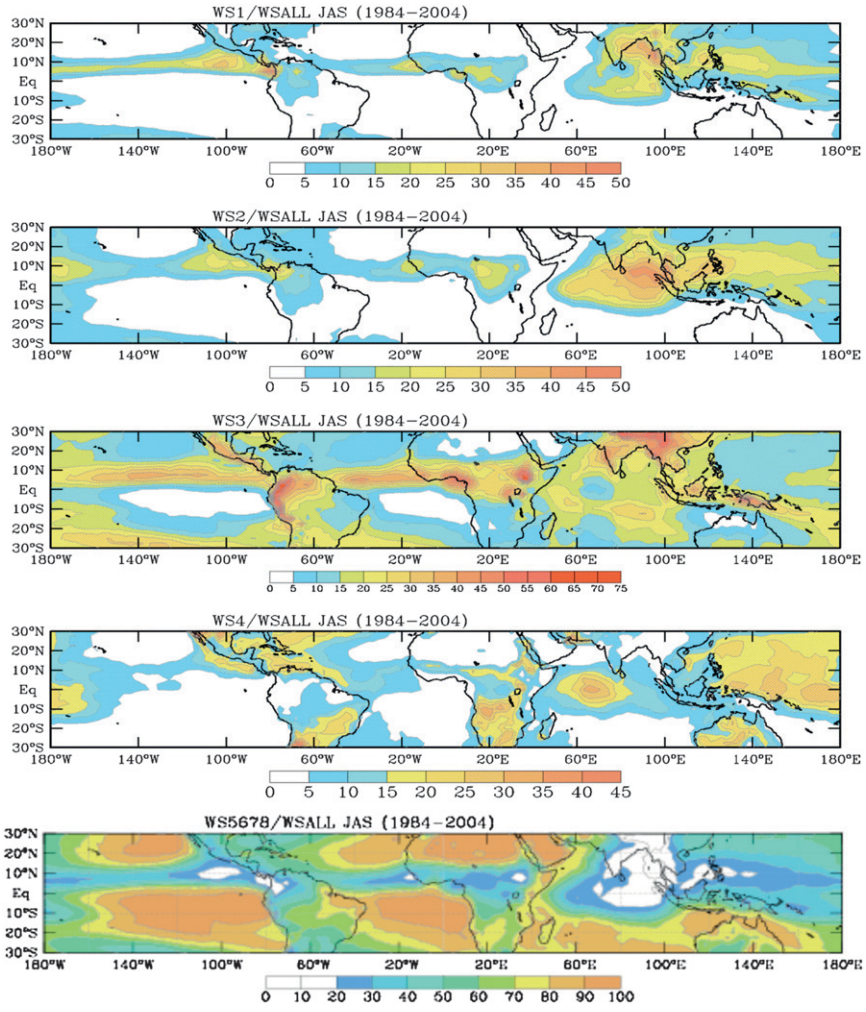

FIG. 3. The geographical distribution of weather states averaged for July–September (over 1984–2004). Percentages are with respect to the total frequency of all weather states (weather state/WS1+ $\cdots$ +WS8). Contours are as shown in the legend of each panel.

on a global 1° horizontal grid. The period of record used here is 1997–2004. Over land this product is a combination of surface gauge measurements and satellite microwave and infrared observations. Details about the GPCP data processing including the statistics can be found in Adler et al. (2003). For a synoptic system, the heating rate associated with 1 mm day^{-1} of rain over 1-m^2 surface area can be calculated using the relationship: $Q = L \times m$, where Q is the heating rate associated with latent heat release, $L = 2.5 \times 10^6$ J kg^{-1}, and m denotes 1 kg of water for an atmospheric column of 1 m^2 (Holton 1992). Based on this assumption, the heating rate associated with 1 mm day^{-1} of rain is about 28.9 W m^{-2} (cf. Holton 1992, p. 388). The latent heating of the atmosphere associated with GPCP rainfall is computed using above procedure.

The full-sky net LW and shortwave (SW) fluxes in the atmosphere (flux divergence) are obtained from the ISCCP flux data (FD) product (Zhang et al. 2004). The ISCCP FD data are reported at 3-h intervals on a 2.5° global horizontal grid. We use daily averages covering 1984–2004.

b. Analysis methodology

We investigate the relationship between the convectively active states and the AEWs over the source region in East Africa and (briefly) downstream in West Africa. Past studies (e.g., MTA06) use time-filtered infrared brightness temperature (T_B) or OLR to isolate AEW-related convection and constructed a basepoint time series index to form a compositing analysis. Here, we base our analysis on the frequency of occurrence of the WS using a kinematic predictor (time-filtered meridional winds) to produce regression composites (see discussion below and section 4) We also use WS as sorting

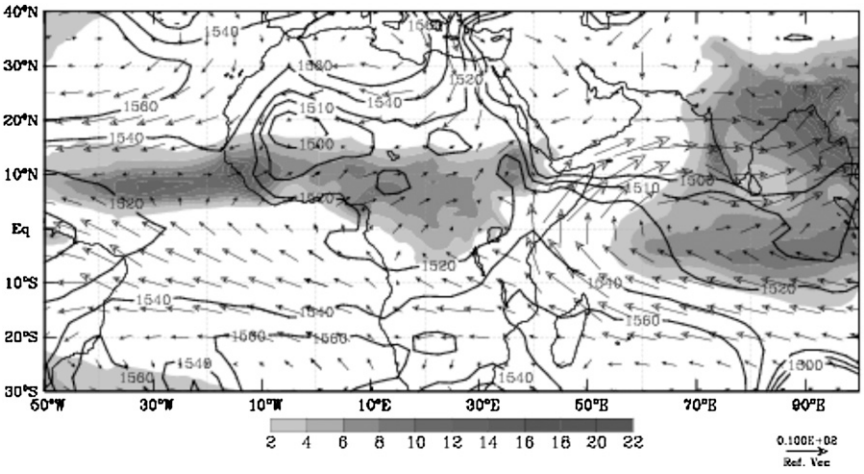

FIG. 4. The distribution of mean July–September GPCP rainfall (1997–2004; shaded every 2 mm day^{-1}), 850-hPa geopotential height (contoured every 10 gpm), and 850-horizontal winds (averaged over 1984–2001, vectors are drawn every 5° for clarity).

criteria to composite dynamical and other variables to investigate wave–convection behavior.

To isolate variations on the time scale of interest, time filtering using a Lanczos filter (Duchon 1979) is applied to the meridional winds. A broader range of variability of AEW is captured by using a bandpass filter of 2–10 days (Dickinson and Molinari 2000; MTA06; cf. KTH06). To sharpen the response of the Lanczos filter, 30-day data points were used on each side of the time series to be filtered.

Composite structures of various quantities are produced using a linear regression based on the 2–10-day-filtered meridional wind variations following Wheeler et al. (2000). Composites are for total fields (e.g., wind, geopotential height, wind divergence, and frequency of WS) correlated and regressed against the 2–10-day-filtered time series index at a chosen location and the results shown in the form of anomalies scaled by one standard deviation of the time series index (also referred to as basepoint time series index or predictor index). We use lag regressions that allow us to examine the evolution of the composite structures. Details of the linear regression procedure can be found in several previous studies (e.g., Kiladis and Wheeler 1995; Wheeler et al. 2000). Note that past studies performed regressions based on wavenumber–frequency-filtered predictors for the study of convectively coupled waves (e.g., Kiladis and Wheeler 1995; Wheeler et al. 2000) including AEWs (KTH06; MTA06). As noted by KTH06, the composite structures of AEWs based on wavenumber–frequency-filtered predictors can be reproduced using time-filtered predictors (as in this study) in a slightly noisier form.

Additionally, we investigate the relationship between AEW dynamics and convection using regression composites based on the WS time series as predictors. We note that the frequency of occurrences of WS variations also show excess variance in the same 2–10-day range (not shown; see RTPJ, their Fig. 3). The procedure for preparing composites in this case is as follows: (i) construct WS1 and WS3 time series indices at a chosen location, and (ii) filter the meridional winds in a 2–10-day window and then regress this onto the WS (WS1, WS3) time series indices. The results are variation structures in the 2–10-day time scale. We also note that the consistency of the statistics from the above exercise was thoroughly checked against composites using basepoint indices at different locations.

3. Climatology

To provide a context for interpreting our results, we briefly review the regional climatology including synoptic- and larger-scale circulation and flow patterns that are relevant to East Africa (see KTH06 for a discussion focused on West Africa). Figure 4 shows the mean rainfall, 850-hPa geopotential height, and winds over Africa and neighboring regions during the July–September season. The figure highlights a broad region of rainfall over North Africa between 5°–15°N, with peaks located over the highlands in Guinea, Cameroon–Nigeria, and Ethiopia. Major features of the mean circulation are the Southern Indian and Southern Atlantic Ocean anticyclones, the anticyclones over Libya and Arabia, and the heat lows between 15° and 20°N. The Sahara (north of about 15°N) is characterized by dry northerly and northeasterly winds. Also shown are moist westerlies and southwesterlies that are collocated with the rainfall zone over tropical Africa and that originate from the high

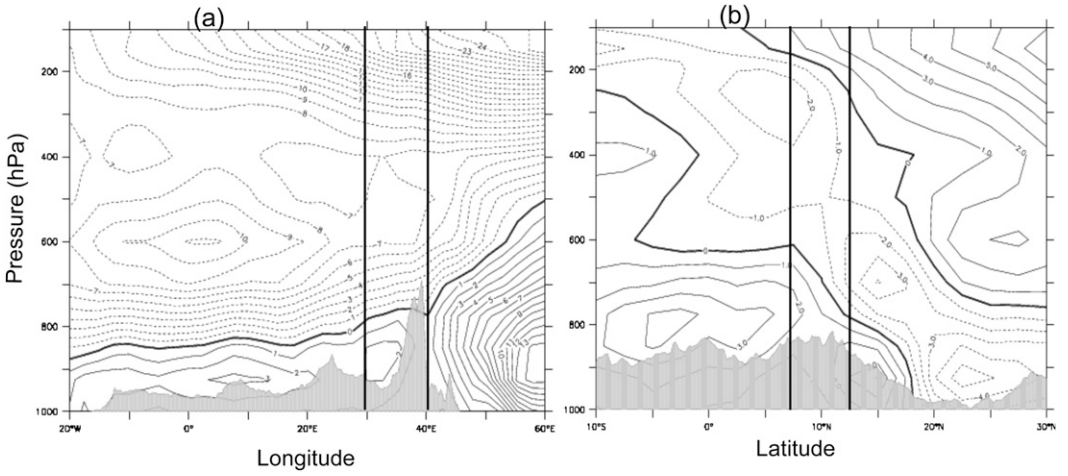

FIG. 5. (a) The pressure–longitude cross section of the mean zonal wind (averaged in 10°–15°N) and (b) the pressure–latitude cross section of the mean meridional wind (averaged in 30°–40°E). Winds are contoured every 1 m s^{-1}. The averages are for JAS 1984–2001. The shading is for elevation cross section. The vertical lines at 30° and 40°E in (a) and at 7.5° and 12.5°N in (b) designate the region of interest.

pressure areas over the southern Indian and Atlantic oceans. The southerlies and southeasterlies from the southern oceans and northerlies and northeasterlies from the anticyclones in the north converge along the heat lows near 15°–20°N over North Africa, referred to as the monsoon trough. Note that convection and peak rainfall are situated to the south of this feature.

Other notable circulation features in the region include strong southerlies and southwesterlies off the coast of Somalia marching toward India (also known as the Somali low-level jet; Findlater 1969). The jet peaks at around the 850-hPa level (~15 m s^{-1}) off the coast of Somalia near 10°N (not shown). This jet is parallel to the East African coast and is not known to contribute to the regional rainfall (boreal summer is a normally dry season for Somalia and eastern Ethiopia).

Also of interest in Fig. 4 are the southerlies and southwesterlies that connect equatorial Africa near the Congo with eastern Africa. The westward moist winds from the south Indian Ocean anticyclone and eastward winds from the south Atlantic anticyclone converge over the Congo basin and appear to flow northeastwards toward Ethiopia. This wind convergence is locally referred to as the Congo air boundary (e.g., Levin et al. 2009; their Fig. 2). Note also the scattered extension of the precipitation zone in this area. This equatorial area is one of the most important regions of convection and large-scale vertical motion (e.g., Eltahir et al. 2004) and serves as the secondary moisture source for convective development. Thus, forecasters in East Africa monitor the moisture variables and wind direction changes over equatorial Africa. Similarly, Cadet and Nnoli (1987) highlighted the importance of the equatorial Atlantic as moisture source for West African rainfall during the summer of 1979, and they speculated that the high rainfall zone of central and equatorial Africa near 30°E as an additional moisture source for the region.

The vertical extent of the African summertime circulation is depicted using cross sections of the horizontal winds. Figure 5a shows the pressure–longitude cross section of the mean zonal wind, averaged over 10°–15°N, which is the peak convective variance zone identified by MTA06 (their Fig. 4a) and the peak rainfall zone during the JAS season (Fig. 4). Prominent features are the easterlies above the 850-hPa level that peak in the AEJ near the 600-hPa level with the westerlies below. The AEJ peaks near the Greenwich meridian, and its amplitude weakens rapidly over the entrance region east of 20°E. The monsoon westerlies are relatively shallow over tropical Africa, but they are much deeper to the east of 40°E, indicating the more vigorous South Asian monsoon (e.g., Krishnamurti and Bhalme 1976). Special note should be taken of the separate tropical easterly jet (TEJ) peaking near 150–200 hPa, extending from Southeast Asia and weakening over tropical West Africa. It will be shown that waves on this jet, distinct from the AEW, play a role in the convection that triggers the AEWs.

Figure 5b shows the pressure–latitude cross section of the mean meridional wind averaged over 30°–40°E. Southerlies are predominant at lower levels (below the 700-hPa level) over the region south of 20°N in East Africa, while northerlies are prevalent at upper levels. Note that the concentration of southerlies to the south and westerlies to the west of the highest mountain ridge

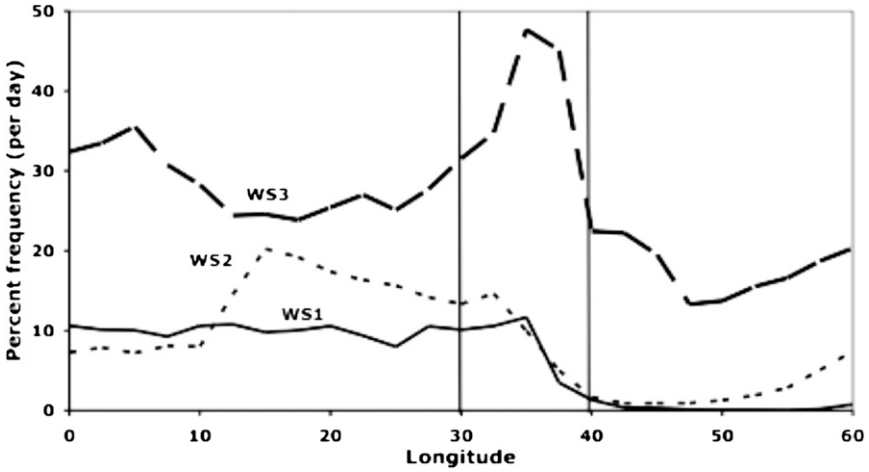

FIG. 6. The longitudinal distribution of the average frequency of occurrences of WS1, WS2, and WS3 averaged in 7.5°–12.5°N (for JAS 1984–2004). The vertical lines along 30° and 40°E denote the area of interest in eastern Africa.

near 40°E are crucial for the monsoonal rains in the region as they carry moisture to enhance the convection (Figs. 5a,b). Over the region north of 20°N, northerlies are seen below the 700-hPa level and southerlies predominate above this level.

4. Deep convection and AEW initiation over East Africa

Past observational studies base their analysis of wave activity and convection using proxy fields such as OLR (e.g., KTH06; Wheeler et al. 2000; Wheeler and Kiladis 1999) or T_B that indicates the coldest top (thick) clouds (e.g., MTA06). Despite plausible features in these results, T_B measurements are known to suffer from cirrus contamination (low T_B may not always correspond to deep convective clouds, rather the satellite could be seeing a cold, nonprecipitating high cirrus cloud). For example, Duvel (1990, 1989) classified clouds into high, medium, and low types based on T_B thresholds and used those cloud categories to study the association of convection with AEWs, but he did not elaborate on the impact of cirrus clouds on his high cloud classification. Tromeur and Rossow (2010) show that OLR does not distinguish between the different kinds of convection that are identified by the ISCCP WS in the tropics. As shown below, the behavior of these different types of convection is different; recognizing this provides new insights to wave–convection interactions.

The longitudinal variations of the average frequency of WS1, WS2, and WS3, across 7.5°–12.5°N, are presented in Fig. 6 (average for JAS 1984–2004). WS3 is the most frequent type of convection over this domain, with a significant peak in frequency at 30°–40°E in East Africa. WS1 and WS2 are less frequent but concentrated to the west of 35°E and almost completely absent to the east.

To document the different roles of each WS in the climatology of atmospheric diabatic heating, we present regression composites of the latent heat release associated with the GPCP rainfall and of the net LW radiative cooling. Composites are formed using daily time series indices constructed based on convectively active weather states (WS1, WS2, WS3) and the convectively suppressed weather state (WS4) at base point 5°–15°N, 30°–40°E over East Africa. A quick look at the simple correlation between rainfall and the frequency of occurrence of convectively active WS shows significant positive correlations, while the correlation between the rainfall and the frequency of convectively inactive states is negative. As discussed in section 2, weather states 5–8 are least frequent over the rainy zone over Africa and we do not discuss them further.

Figure 7 shows composite anomalies of latent heat release (anomalies are with respect to the JAS 1997–2004 average) with respect to WS1, WS2, WS3, and WS4 time series indices at the base point indicated above at day 0 (the time of maximum frequency of occurrence of each WS). The results are averaged over 5°–15°N. By far, the largest contribution (60–70 W m^{-2}) to the latent heating over East Africa (30°–40°E) comes from WS1 (stronger convection associated with MCSs) followed by WS2 (associated with anvil clouds). The contribution associated with WS3 is much smaller compared with WS1 and WS2, although this cloud type is the most frequent over East Africa (cf. Figs. 3 and 6). Almost equally strong latent heating associated with WS1 and WS2 is seen over the high terrain in Ethiopia, just west of 40°E. However, the convective heating associated with WS1 dominates while

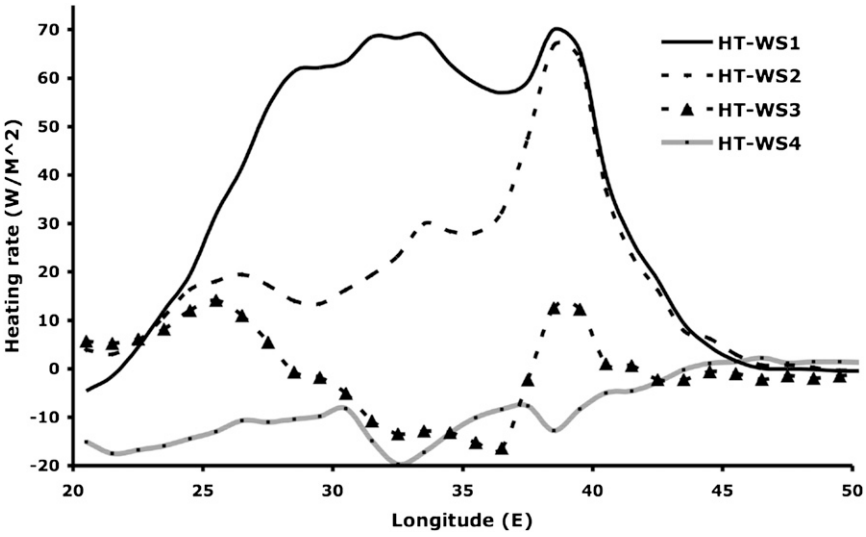

FIG. 7. The latent heat release (computed from GPCP rainfall) regressed against weather states (WS1, WS2, WS3, and WS4) at the base point 5°–15°N, 30°–40°E at day 0, the time of maximum relative frequency of occurrences of weather states, for Central and East African region (averaged in 5°–15°N). The latent heating associated with each weather state is shown in the legend.

the contribution from WS2 decreases over the region 25°–35°E, west of the Ethiopian highlands. Figure 7 also shows that the latent heating anomaly associated with WS4 (cirrus clouds) is 10–20 Wm^{-2} below the average.

Figure 8 shows net LW flux anomalies in the atmosphere. Note that the mean net LW flux in the atmosphere for the JAS is negative (not shown), indicating net cooling, so a positive anomaly is a heating of the atmosphere. (Mean maps for net LW flux in the atmosphere can also be obtained from the ISCCP Web site at http://isccp.giss.nasa.gov/projects/browse_fc.html.) Radiative cooling of the atmosphere decreases when convectively active clouds are present, particularly over the region west of 35°E where the WS1 and WS2 frequencies increase. In general, the role of WS3 is not as radiatively important compared to the other convectively active clouds over this region, although slightly increased cooling is seen over 30°–40°E (Ethiopian highlands). We will show later that WS3 has a greater role when they interact with the Ethiopian highlands compared with WS1. The effect of cirrus clouds (WS4) on the LW cooling is small, except for the region east of 35°E, where WS4 is associated with a slightly more cooling.

Comparison of Figs. 3 and 4 shows that WS1, WS2, and WS3, which are associated with convectively active cloud regimes, are most frequent within the zone of peak rainfall during the JAS season. Figure 7 reinforces the conclusion that the latent heating is produced primarily by these WS. Since the peak rainfall over tropical Africa is the region where high AEW activity is known to be related to moist convection south of 15°N (e.g., Thorncroft and Hodges 2001), we use the WS to describe convection variation over the region. However, since the JAS frequency distribution for WS1 and WS2 over tropical Africa is similar (see Fig. 3) and since subsequent computations showed similar structures, we will use only WS1 and WS3 in further displays. To explore the statistical relationship between AEW phases and convective activity, we construct a basepoint time series index using 2–10-day bandpass-filtered 700-hPa meridional wind at 12.5°N, 30°E in East Africa, the source region of AEWs. Therefore, unless otherwise indicated, regression results are anomalies scaled by −1 times the standard deviation of this basepoint time series index. The rationale for scaling by −1 is to evaluate WS anomalies with respect to northerly anomalous winds at day 0 in the center of the Hovmöller figures below.

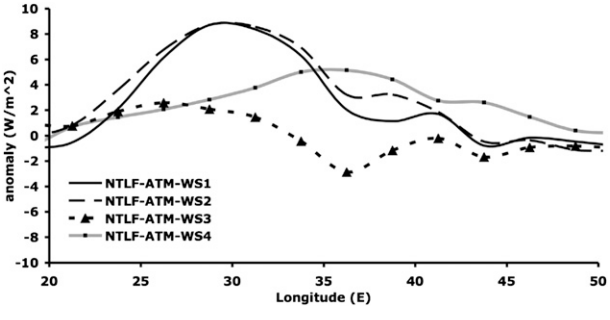

FIG. 8. The net longwave fluxes in the atmosphere (NTLF-ATM) for full-sky regressed against weather states at the base point 5°–15°N, 30°–40°E at day 0 (averaged in 5°–15°N). The radiative flux associated with each weather state is shown in the legend.

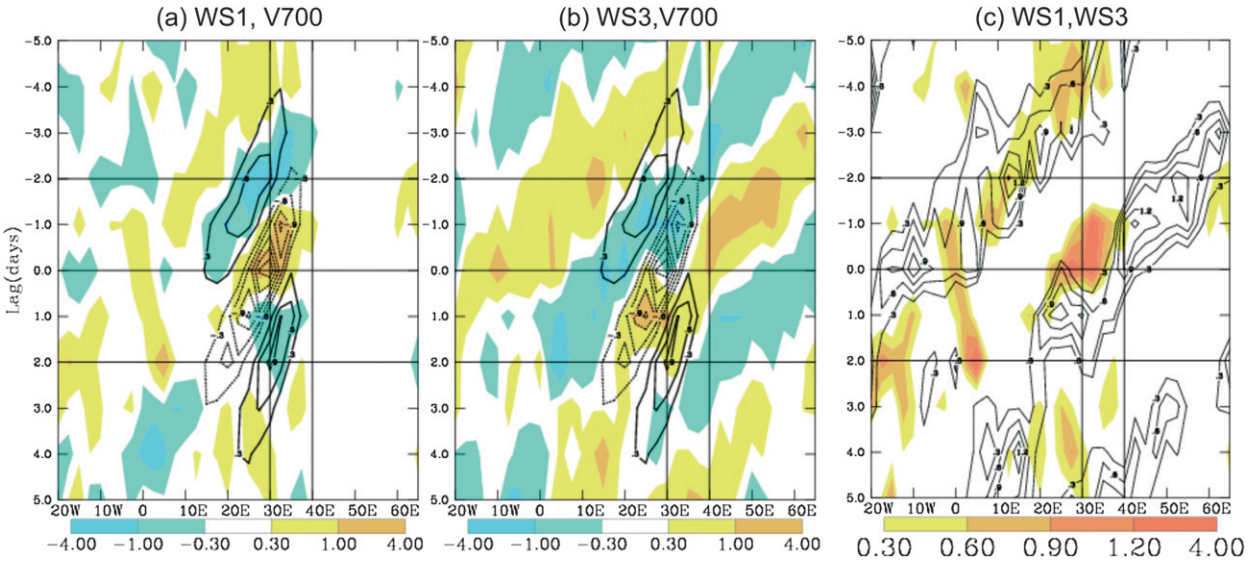

FIG. 9. The frequency of occurrence of weather states and 700-hPa meridional wind projected onto 2–10-day-filtered 700-hPa meridional wind at 12.5°N, 30°E; (a) WS1 and meridional wind, (b) WS3 and meridional wind, and (c) WS1 and WS3. Anomalous WSs in (a) and (b) are shaded as shown in the legend (see Fig. 6 for average frequency of WSs). WS1 anomalies in (C) are shaded and WS3 are contoured (only positive anomalies are shown for clarity). Anomalous WS occurrences are in percent per day. Anomalous meridional winds are contoured every 0.3 m s^{-1} (positives solid and negatives dashed). The cross sections are for 7.5°–12.5°N. Vertical lines at 30° and 40°E denote the area of interest.

a. Convectively active clouds regimes and dynamical measures of AEW

Figures 9a and 9b show the time–longitude cross sections of WS1 and WS3 and the 700-hPa meridional wind anomalies all projected onto the basepoint time series index (averaged over 7.5°–15°N latitudes; WS anomalies are shaded and wind anomalies are contoured). Generally, the WS anomalies and the dynamical structures show coherent westward-propagating features with a clear link between West and East Africa. The positive anomalies of the WS1 occur in association with the northerly wind anomalies from 40°E westward to about 25°E where the relationship ends. The relationship between WS3 and the AEW is more complicated, especially over the Ethiopian highlands (near 30°–40°E), where it is initially related to the southerly wind anomaly. However, as the AEW grows in strength, WS3 shifts to association with the northerly wind anomaly as WS1 decays at about lag +1 day. Note that the propagating WS3 anomaly is just as strong to the east of the beginning of the AEW wind anomaly.

Comparison of Figs. 9a and 9b shows important differences in the east–west structures of WS1 and WS3. The WS1 anomalies are confined to the region west of 40°E, while their signature to the east is much weaker (cf. Fig. 6). Larger WS1 anomalies (cf. Figs. 2 and 3) are seen between the Ethiopian highlands and central Africa near 15°E (see Fig. 1 for orientation) between day −2 and day 0. Although the WS1 anomalies are smaller between day 0 and day 2, they increase again over West Africa, west of 10°E, around day 2 (Fig. 9a). In contrast, negative WS3 anomalies are coincident with the northerly anomalies over Ethiopian highlands between day −2 and day 0, while positive WS3 anomalies are seen with southerly anomalies between day 0 and day 2 over the same location. However, over the region west of 30°E, positive WS3 anomalies are associated with northerly anomalies.

In general, over West Africa, in the region where the AEW signature amplifies, the AEW–convection relationship is different than in the east. Past studies showed that convective activity increases under northerly wind anomalies in the vicinity of the trough or to the west of it, while they tend to weaken to the east of the trough (e.g., KTH06; Reed et al. 1977). Also, based on the satellite imagery available to them at the time, Reed et al. (1977) showed that the percentage cover of ''white appearing clouds'' that represent convection increase ahead of the 700-hPa trough axis. This led them to conclude that convection is mainly modulated by the easterly waves. We see those same relationships over western Africa but found that the relationships are different and more complicated over East Africa, where wave signatures are very weak.

A notable feature of the WS3 anomalies (isolated and smaller-scale weather states) is that they can be traced as far east as the Arabian Sea and as far west as the eastern Atlantic Ocean (Fig. 9b). In a study based on

space–time-filtered T_B, MTA06 also found traces of coherent convective structures that originate near the western Arabian Sea and that reach West Africa (their Fig. 12). This is also consistent with operational forecasting experience in East Africa (Tadesse 1994). In his study on the impact of the Arabian Sea storms and disturbances on Ethiopian rainfall, Tadesse (1994) indicated that intense convective clouds that form over the Yemen highlands and western Arabian Sea propagate westward and have an important role in enhancing convective activity over Ethiopian highlands. Furthermore, studies (e.g., MTA06) have shown that convective activity that is organized over East African highlands is important for AEW initiation to the west. Lin et al. (2005) noted that the AEW that was associated with hurricane Alberto in 2000 was linked to mesoscale vortices over Ethiopian highlands.

The AEW anomalies east of 35°E are not significant, but there is a significant positive WS3 anomaly to the east of this region. In other words, the unorganized form of convection is enhanced even though AEW is nonexistent to the east of the Ethiopian highlands. The fact that the convectively active cloud regime, WS3, precedes the wave signal over East Africa suggests that this anomaly of deep convective activity is a precursor for AEW initiation downstream (e.g., MTA06; KTH06).

Inspection of Figs. 9a and 9b also shows that the WS anomalies exhibit slightly different propagating speeds west of 30°E: to the east, the WS3 anomaly propagates at a relatively faster speed but slows down over the Ethiopian highlands, whereas to the west, the WS1 anomaly appears to propagate a little faster than the AEW until it decays but the WS3 anomaly follows the AEW with a significant phase shift after the WS1 anomaly disappears.

The low-level (surface to 700 hPa) mean flow over the region off the coast of Somalia and over western Arabian Sea is predominantly westerly (Fig. 4). A quick examination of the relationship between zonal winds at 5°–15°N, 50°–60°E, just off the coast of Somalia, and the global frequency of occurrences of WS suggests a positive correlation (not shown) over the Arabian Sea and western Indian subcontinent. Given this, it may seem implausible that the convection that is generated either in this region or farther east could propagate westward. However, it is also noteworthy that the mean flow above the 700-hPa level is dominantly easterly, suggesting that the westward propagation of convection is steered by the upper-level flow.

We also note that WS1 and WS3 peak at somewhat different geographic locations even at the same lag times indicating a more intricate interaction between the two types of convection. This is shown more clearly in Fig. 9c, where WS1 and WS3 anomalies are reproduced to aid visualization (only positive anomalies are shown for clarity; WS1 anomalies are shaded and WS3 anomalies are contoured). The sequence of events begins with a positive WS3 anomaly over the Arabian Sea that propagates westward to the Ethiopian highlands from day −3 to day 0, with the largest amplitude and a change in propagation speed appearing just to the east of 40°E. Note that the ridge of these highlands is located just to the west of 40°E (cf. Fig. 5a). A positive WS1 anomaly then appears just to the west of 40°E between day −1 and day 0, while WS3 amplitude weakens over the highlands. This switch from WS3 to WS1 coincides with the appearance of a significant AEW signal in the meridional winds (cf. Figs. 9a and 9b). To elucidate the details of how WS3 transitions to WS1 over the highlands and initiates the AEW to the west requires an analysis with higher space–time-resolution observations to resolve the role of the topography and the diurnal variations of convection; this will be examined in a companion study.

Figure 9c also shows another transition farther west. As the AEW wind anomaly strengthens moving west to 25°E by day +1, the WS1 anomaly weakens and the WS3 anomaly strengthens again but jumps from a location near 35°–25°E. The reinvigorated WS3 anomaly continues to move westward with the AEW until at least day +3 reaching 10°–15°E. In general, when the WS3 signal weakens, a pulse of WS1 (and WS2; not shown) positive anomaly appears. The role of AEWs in this process is not clear at this stage (cf. Figs. 9a,b). Recall that the AEW attains maximum amplitude over West Africa. Several studies (e.g., Reed et al. 1977) have shown that low-level convergence and cyclonic vorticity increase ahead (to the west) of the midtropospheric AEW trough, which is important for convective cloud growth. This implies that scattered convective clouds (represented by WS3) become more organized WS1 type, at least in part, in association with the easterly waves over West Africa. However, it appears to be the perturbation caused by the propagating WS3 anomaly, steered by the upper-level winds, that triggers a WS1 event that initiates the AEW in the east.

The east–west tracks of the wind and WS relative frequency anomalies shown here are weaker and shorter over West Africa compared with past observations that use OLR (e.g., KTH06). This is due, in part, to differences in the location of time series basepoint indices, but also due to the fact that the OLR signal combines WS1, WS2, and WS3 and perhaps some elements of WS4. To check this point, a sensitivity test was performed using the 2–10-day-filtered 700-hPa meridional wind at 7.5°N, 5°E in West Africa (a region where 2–10-day 700-hPa meridional wind variance peaks locally). Results from this (not shown) indicate the presence of a coherent east–west propagation of convection connecting East and West Africa. The structures based on this West African

base point are longer in their east–west tracks, consistent with previous studies. We also note that WS3 anomalies in the region 10°–30°E are weaker, but stronger over West Africa, west of 10°E. WS3 signatures are also evident east of 40°E, consistent with Fig. 9b.

Overall, the results described above suggest that the WS3 anomaly precedes the large-scale wind anomalies over East Africa, suggesting that this enhanced convection plays a role in the AEW genesis. The results also indicate that the relationship between WS anomalies and AEW activity over East and West Africa are different. Whereas positive WS anomalies increase in the vicinity of an AEW trough over West Africa, convection over the east is little modulated by (weak) AEW disturbances. The remaining questions are as follows: what causes the enhancement of convection over regions to the east of Africa and how does the convection get organized over the region 30°–40°E? The details of this are examined using additional dynamical variables below.

For completeness, we also examined the relationship between WS4 and the meridional wind anomalies (not shown). In general, positive anomalies of WS4 appear to increase with southerly anomalies (i.e., to the east of the 700-hPa trough axis). Negative WS4 anomalies seem to be in phase with northerlies. Comparison of WS1, WS2, and WS3 anomalies (convectively active cloud regimes) against WS4 anomalies (convectively suppressed cloud regimes) also indicate that the former peak before the latter, suggesting the evolving nature of high cirrus out of deep convection. These differences emphasize that a T_B- or OLR-based analysis, which mixes all these WS together, would not see the detailed behavior we have illustrated above.

b. *Role of moisture flux divergence, upper-level wind divergence, and upper-level easterly waves on convectively active clouds over East Africa*

Increasing convection over a region may be related to increasing low-level moisture flux into that region. To investigate this possibility, the zonal and meridional moisture flux divergences are regressed onto the basepoint index used above.[2] Because the monsoon flow over Africa is shallow (Fig. 5) and water vapor is concentrated in the lowest layers of the troposphere (Cadet and Nnoli 1987), the 850-hPa level is chosen (note that most of East Africa is above 1000 m above mean sea level, cf. Fig. 1).

Figures 10a and 10b show the time–longitude structures of the regressed anomalies of 850-hPa moisture flux divergence. Dashed contours (negative magnitudes) denote moisture flux convergence over the area, whereas solid contours (positive magnitudes) denote moisture flux divergence. The frequencies of occurrence of WS1 and WS3 are superimposed (shaded). Over the region near 30°–40°E, positive anomalies of WS1 are collocated with moisture flux convergence, an important aspect of low-level conditioning for the development of organized convection, while most of the negative WS1 frequency anomalies are associated with the moisture flux divergence.

The relationship between WS3 anomalies and moisture flux convergence is more complicated (Fig. 10b). Over the region near 30°–40°E, negative WS3 anomalies are associated with moisture flux convergence between day −2 and day 0. Also, weak but positive WS3 anomalies are collocated with moisture flux divergence between day 0 and day +2 over this location. This is coincident with a weakening of WS3 positive anomaly over the Mountains and subsequent shift in the peak of the positive WS1 anomalies at day −1 (Fig. 9c) and the appearance of the AEW signature (Figs. 9a,b) noted earlier. Perhaps, weakening of the WS3 anomaly is related to the fact that the low-level moisture flux convergence favors the WS1 type over the mountains just to the west of 40°E. However, we caution that some of the mountains over Ethiopia (35°–40°E) exceed 2500 m above sea level and the 850-hPa level wind field from the ECMWF reanalysis may not adequately describe the circulation in this mountainous region. In contrast, over the region to the west of 30°E, negative WS3 anomalies are associated with moisture flux divergence between day −2 and day 0, while positive anomalies are seen in the vicinity of the moisture flux convergence between day 0 and day +2. Note that the moisture flux convergence appears to propagate at a slower speed (~6 m s^{-1}) compared with the WS (7–9 m s^{-1}). A careful inspection also indicates that the peak moisture flux convergence anomaly slightly precedes the maximum positive frequency of WS1 in the region 30°–40°E, suggesting that moistening of the lowest layers of the troposphere favors increased WS1-type activity.

An upper-tropospheric wind divergence is also generally associated with increasing upward motion and convection (and a horizontal wind convergence in the lower levels of the troposphere as a consequence of mass continuity). Figure 11 shows the 200-hPa level wind divergence field projected onto the same basepoint index used above with the WS anomalies superimposed for easy comparison (zoomed into the region between 0° and 60°E for clarity). Positive WS1 anomalies are associated with 200-hPa wind divergence near 30°–40°E, suggesting that

[2] Daily values of zonal and meridional moisture flux divergence are computed separately and combined to form composite anomalies (see Fig. 10). The relative magnitudes of each of the zonal and meridional flux over the area of interest are in the same range.

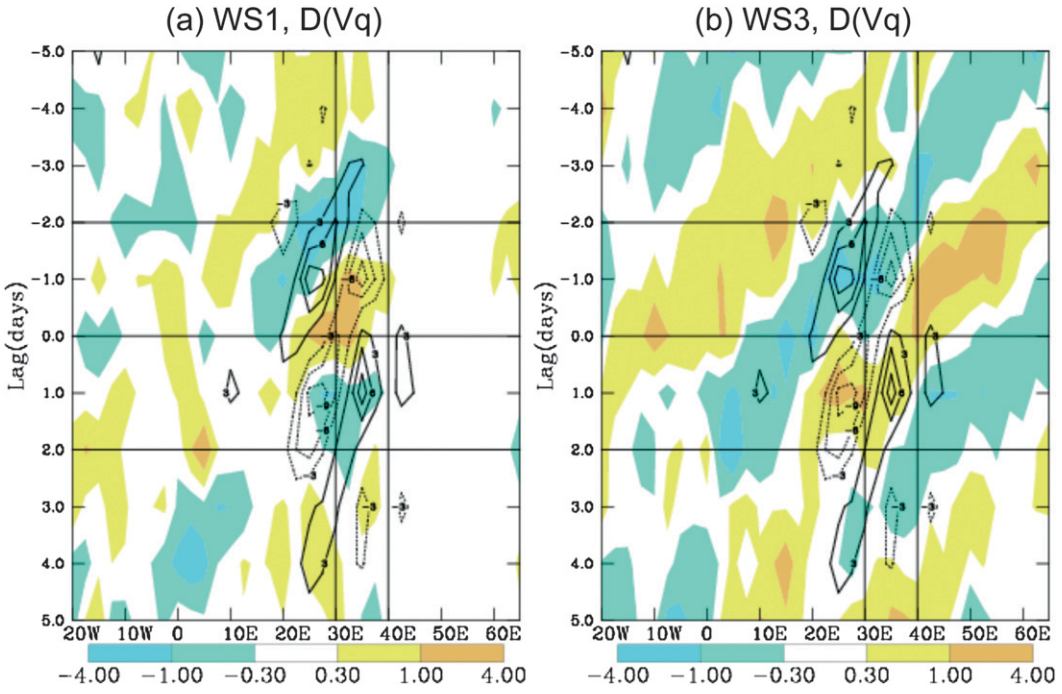

FIG. 10. (a),(b) As in Fig. 9, but for 850-hPa moisture flux divergence. Contours are drawn every 3×10^{-6} s^{-1} g kg^{-1}(solid contours, positive values, represent moisture flux divergence and dashed contours, negative values, represent moisture flux convergence). Moisture flux divergence are computed using $[\partial(uq)/\partial x + \partial(vq)/\partial y]$, where u and v are horizontal winds, and q is the specific humidity. The cross sections are for 7.5°–12.5°N.

the upper tropospheric wind divergence influences convective development or results from the convection. Negative WS1 anomalies are, mainly, associated with upper-level wind convergence. As pointed out earlier, the WS3 anomalies and upper-level wind divergence anomalies seem to have a complicated relationship over East Africa. However, in general, over the region immediately to the west, positive WS3 anomalies seem to be in phase with upper-level wind divergence between day 0 and day +2. Figure 11 also indicates that positive WS1 anomalies and upper-level wind divergence anomalies are in phase over West Africa, west of 10°E. Further comparison of Figs. 10 and 11 indicates that the maximum moisture flux convergence occurs about 12–24 h earlier than the maximum upper-level wind divergence (over 30°–40°E), implying that moistening of the low levels of the atmosphere leads to stronger convection (WS1) and upper-level wind divergence.

To further investigate the mechanisms in the development of convective activity, we examine the relationship with the upper-tropospheric easterly waves, which may provide an additional dynamic impetus for convective system development. Based on observational data, Krishnamurti (1971) showed the presence of easterly waves in the upper troposphere in association with the upper-level TEJ that extends between South Asia and tropical Africa. This jet and its waves are distinct from the AEJ and AEW. Burpee (1972), based on observational data, states that these two jets are indeed ''distinct and separate.'' He suggested that the TEJ observed over East Africa is a ''remnant of the Indian monsoon jet.'' As discussed earlier, the AEW structure over East Africa is weaker and much less coherent compared with the upper-level wind structures (cf. Fig. 12). The generation process of the upper-level easterly waves and the AEW are also different (see discussion above). While the upper easterlies are triggered in association with unstable TEJ (e.g., Krishnamurti 1971; Mishra and Tandon 1983), our results show that AEW are initiated by convection over East Africa even if their subsequent amplification over West Africa is supported by the AEJ mechanism (e.g., Burpee 1972; Leroux and Hall 2009).

Mekonnen (2007) suggested that the upper-level easterly waves have an important role in enhancing 3–4-day convection over East Africa. To explore this, we lag regressed the 200-hPa meridional wind and the frequency of the WS against 2–10-day-filtered 200-hPa meridional wind at 12.5°N, 30°E (the same geographic location used above). As seen in Fig. 12, the wave amplitude increases westward and the northerly anomalies peak near 30°E at day 0, as expected. The waves can be traced as far east as the northern Indian Ocean and Bay of Bengal region.

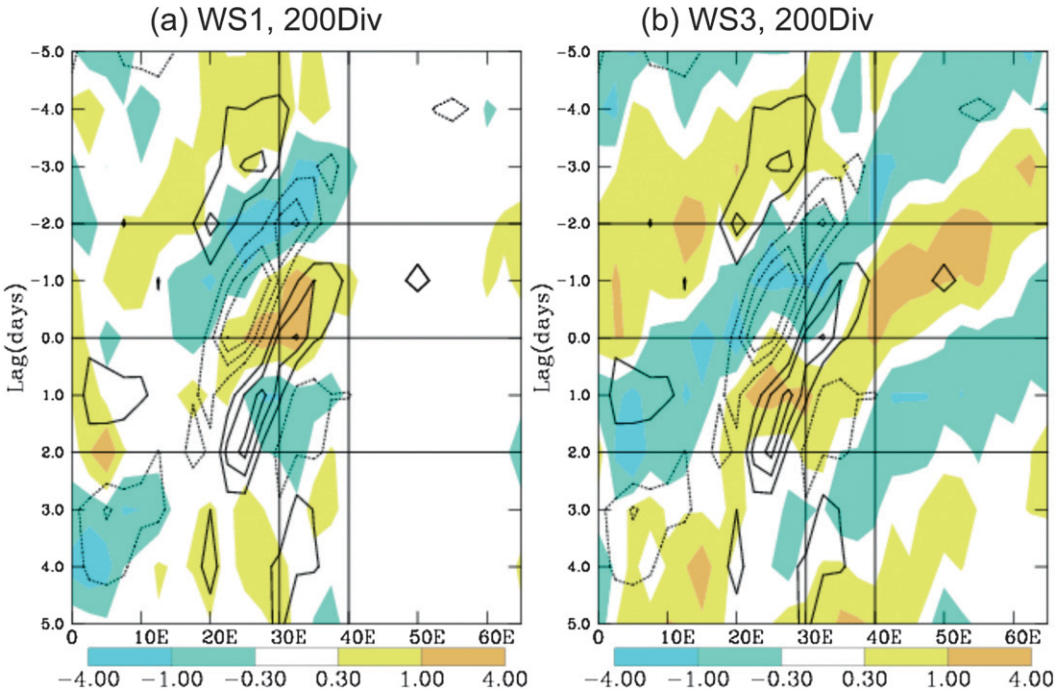

FIG. 11. (a),(b) As in Fig. 9, but for 200-hPa wind divergence. Contours are drawn every 2×10^{-7} s^{-1} (solid contours are for wind divergence and dashed contours for wind convergence). The cross sections are for 7.5°–12.5°N.

These waves are characterized by an approximately 4-day periodicity, 14 m s^{-1} phase speed, and 4800-km wavelength, consistent with the observations of Krishnamurti (1971). It is interesting to note that positive frequency anomalies of WS1 and WS3 are mainly associated with the upper-level northerly anomalies, while negative WS anomalies are associated with upper southerly anomalies over the region west of 60°E. This is consistent with the findings of KTH06, who showed that synoptic-timescale OLR-based convection increases when upper-level northerly anomalies are present over West Africa. It is also seen that WS1 anomalies are confined to the region west of 40°E, while WS3 anomalies are seen to the east of this, consistent with our earlier findings (Figs. 9a,b). Overall, these results suggest that upper-level easterly waves play a role in enhancing the WS3-type convection over the Arabian Sea and steering the enhanced convective activity into the 30°–40°E region. The upper-level easterly wave–convection relationship east of the study area is beyond the scope of this work.

c. *Vertical structure*

We now explore the relationship between dynamical quantities and convective systems using the relative frequency of occurrences of WS as predictors. First, the meridional winds from surface to 100 hPa are Lanczos filtered in the 2–10-day range to isolate the easterly wave component in the total wind field. Second, composites are formed by projecting the filtered meridional winds onto a base-point index constructed at 7.5°N, 35°E using the frequency of occurrences of the WS. The choice of this base point is related to the fact that the local frequency maximum in East Africa occurs near this point (see Fig. 3). Although the sorting is performed using all three convectively active weather states, we present the vertical profiles based on WS1 and WS3. The basis for this is our interest in the evolution of convectively active clouds with longer east–west structures (see Figs. 9a,b).

Figure 13 shows the pressure–longitude profile of filtered meridional winds regressed onto the WS1 time series index at the base point. To study how the variation of WS3 change with the variations of WS1, the frequency of occurrences of WS3 is also regressed onto the WS1 index at the same base point (shown at the bottom panels in dashed lines) for day −2 through day +2. In addition, the frequency of occurrences of WS1 is regressed onto WS1 index and results are plotted along with composite anomalies of WS3 (bottom panels in solid lines). Similarly, Fig. 14 shows the pressure–longitude profile of filtered meridional wind but regressed against WS3 time series index at the same location between day −2 and day +2.

A common feature in Figs. 13 and 14 is that the meridional wind anomalies in the upper troposphere are much larger than the anomalies in the lower troposphere and the structures are vertically aligned. As shown in Fig. 13, over the region 30°–40°E, weak southerly anomalies

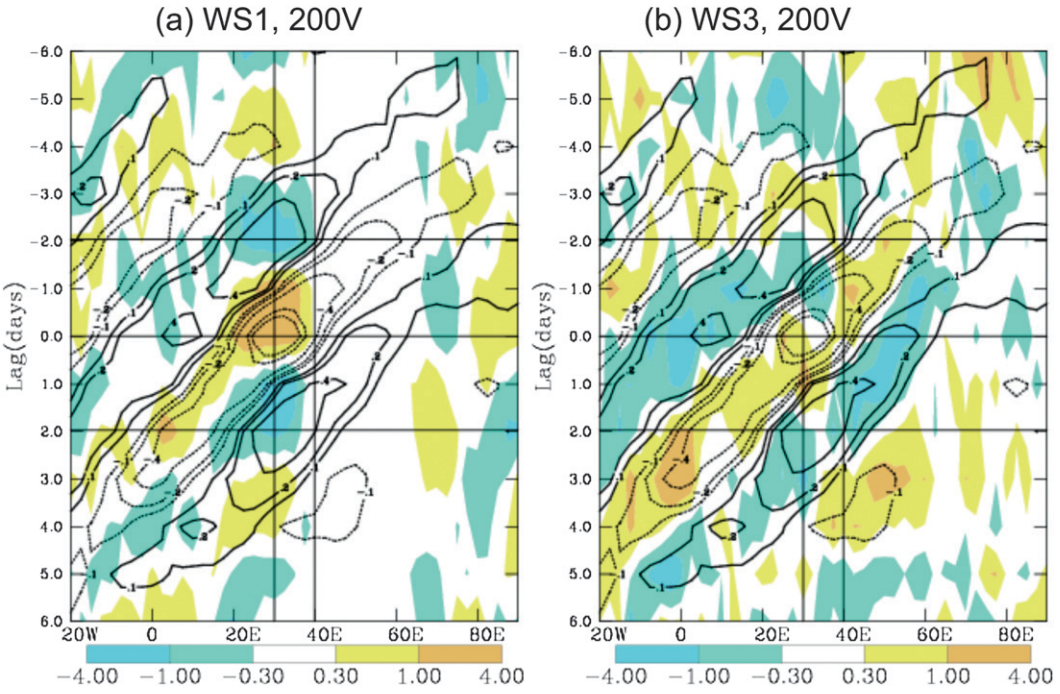

FIG. 12. (a),(b) The frequency of occurrence of WSs and 200-hPa meridional wind projected onto 2–100-day-filtered 200-hPa meridional wind at 12.5°N, 30°E. WS anomalies are shaded as shown in the legend. Anomalous meridional winds are contoured in steps of 0.1, 0.2, 0.4, 0.6, 0.8, and 1.0 m s^{-1} (southerlies solid and northerlies dashed). The cross sections are for 7.5°–12.5°N; (a) WS1 and meridional wind and (b) WS3 and meridional wind.

above the 700-hPa level at day −2 shift to northerly anomalies by day 0 and the corresponding WS1 anomaly increases substantially. On day +2, the northerlies move westward and are replaced by the southerly anomalies with the WS1 anomalies decreasing rapidly. As seen in bottom panels, the WS3 anomalies change in the opposite sense to the WS1 anomalies during the same time period. We note that at day −2, WS3 anomalies are positive east of 40°E but weaken by day 0 over the East African mountains, then slightly increase again downstream over West Africa by day 2. This is consistent with the earlier evidence shown in Figs. 9–11.

In contrast, Fig. 14 (based on WS3 time series index) shows that the region between 30° and 40°E is characterized by southerly anomalies between surface and 700 hPa and by northerly anomalies between 700 and 300 hPa at day 0. The WS3 anomalies peak at day 0 but subsequently weaken over West Africa. The difference in vertical structure seen in Figs. 13 and 14 can be attributed to the fact that WS1 is less frequent at the anchor region, while WS3 is most frequent there (see Fig. 3). It is no surprise that WS1 regressed against the WS1 index (Fig. 13) and WS3 regressed against the WS3 index (Fig. 14) show above-average anomalies at day 0. However, WS3 regressed against the WS1 index in Fig. 13 and WS1 regressed against the WS3 index in Fig. 14 indicate below-average anomalies at day 0; recall that when WS3 is most frequent, WS1 is least frequent. This behavior confirms the interpretation of the previous analysis in terms of a switching between these two types of convection. Also, the amplitude of synoptic-scale wind anomalies in the upper troposphere appears to be slightly larger in Fig. 13 compared with Fig. 14. This indicates a stronger interaction of the waves with deep MCSs (WS1) than with a smaller-scale isolated regime (WS3), again, consistent with the previous results.

In general, the vertical structures found here are somewhat different from some earlier work based on West Africa (e.g., KTH06). This should be expected because the tilt in the meridional wind vertical profile over West Africa is likely to be related to the presence of strong baroclinicity in the region as a result of horizontal temperature gradient between the hot Sahara to the north and cold equatorial Atlantic sea surface temperature to the south. KTH06 showed a different vertical orientation of meridional winds based on anchor points in the rainy zone at 10°N, 10°W and to the north of this at 15°N, 17.5°W. However, since their analysis was limited to the region west of 20°E, we cannot make any further comparison with our results. The nature of such vertical structure orientation over the East Africa is not well understood, but we speculate that the vertical profile of

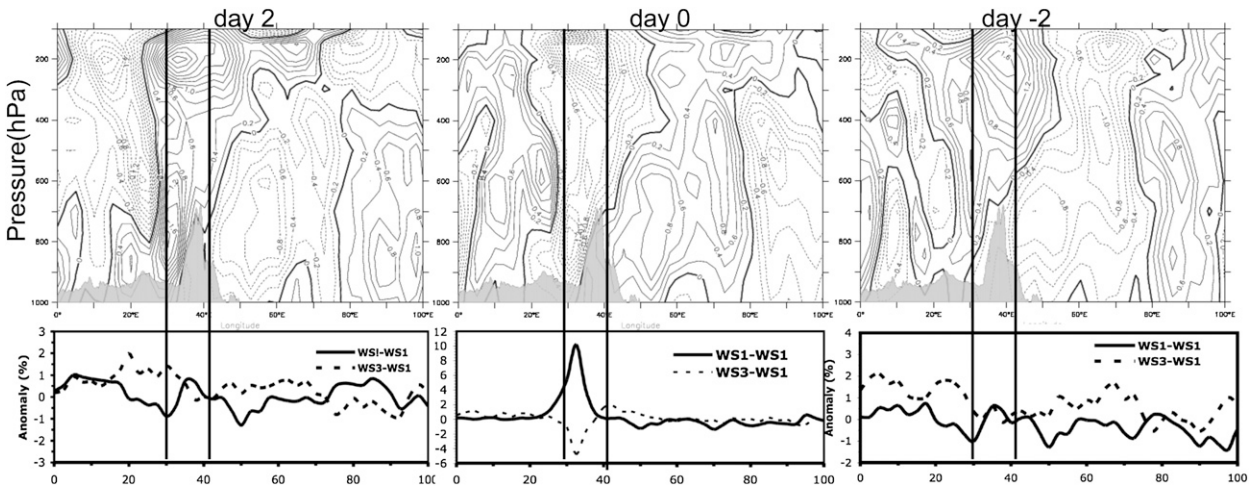

FIG. 13. (top) The pressure–longitude cross section of 2–10-day-filtered meridional wind regressed onto the frequency of WS1 at 7.5°N, 35°E for day −2 to day 2 is represented. (bottom) WS1 (thick-solid line) and WS3 (dashed) regressed onto the same WS1 frequencies at the base point are presented. The gray shading in the upper panels represents the elevation cross section. Meridional winds are contoured every 0.02 m s^{-1} (dashed are for northerlies and solid for southerlies). The vertical lines at 30° and 40°E delineate the area of interest. The cross sections are at 7.5°–12.5°N.

the meridional winds is more vertically uniform as shown here because the north–south temperature gradient over East Africa is not as large as that seen over West Africa (not shown). In addition, the difference between our results and KTH06 is related to the choice of geographic location and more importantly, due to the fact that we use the daily frequency of occurrences of WS while KTH06 used space–time-filtered OLR, which mixes the different convective types along with some cirrus clouds.

An additional point of interest is that the meridional wind anomalies associated with the WS are weaker at lower levels and stronger at the upper levels, suggesting a more important role of the upper-level easterly wave disturbances in affecting the convective systems over East Africa. The fact that wind perturbations at lower levels are weak also confirms the previous results that show easterly wave disturbances over the east are weak.

5. Summary and final comments

Most of the past studies of deep convection and AEW focused almost exclusively on West Africa for various

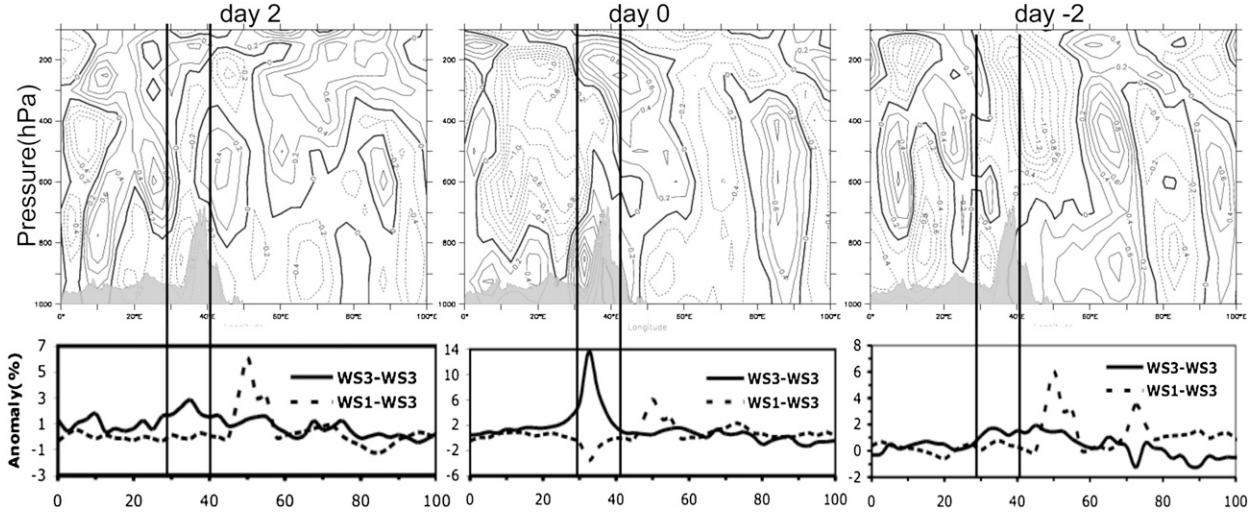

FIG. 14. (top) The pressure–longitude cross section of 2–10-day-filtered meridional wind regressed onto the frequency of WS3 at 7.5°N, 35°E for day −2 to day 2 is presented. (bottom) WS3 (thick-solid line) and WS1 (dashed) regressed onto the same WS3 frequencies at the base point are presented. The gray shading in the upper panels represents the elevation cross section. Meridional winds are contoured every 0.02 m s^{-1} (dashed are for northerlies and solid for southerlies). The cross sections are at 7.5°–12.5°N.

reasons, one being the scarcity of observations over the east compared with the west. Satellites can now mitigate this problem. We used the ISCCP WS database, the ISCCP radiative flux product, and precipitation from GPCP to fill this gap. One clear advantage of the ISCCP WS product is that it distinguishes different types of convective activity as well as separating convectively active and inactive situations, whereas the OLR used in previous studies does not separate these situations.

Composite analysis shows that stronger latent and LW radiative heating anomalies in the atmosphere are produced by the stronger, mesoscale-organized convective activity represented by WS1, whereas the smaller-scale, unorganized convective activity represented by WS3 produces much weaker diabatic heating, even though it occurs much more frequently. Thus, any transition from WS3 to WS1 implies a stronger heating of the atmosphere, similar to the situation studied by Tromeur and Rossow (2010).

The regression composites based on 2–10-day-filtered 700-hPa meridional winds at an East African location show coherent westward propagation of convective (WS) and meridional wind anomalies. Over central and West Africa, the more frequently studied case, the convective anomalies, particularly the WS3 type, and the AEW propagate with a similar phase speed, indicating strong coupling between the AEW and the convection. Over the east, however, the convective anomalies appear to propagate at a slightly larger phase speed compared with the wind anomalies, consistent with the waves being in the early stages of growth. The analysis here clearly shows that the WS3 anomaly, arising over the Arabian Sea and western Indian Ocean, precedes the AEW signal; in fact, WS3 convection increases over the east a day or two before the maximum northerly wind anomaly occurs over East Africa, in agreement with earlier studies that suggested that AEWs are forced by convection over the east (e.g., Berry and Thorncroft 2005; MTA06; THK08). A specific feature of our results is that it is an anomalous enhancement of the less-organized (weaker) convection (WS3) type, steered by the upper-level winds, that appears to initiate events; when the WS3 anomaly reaches the Ethiopian mountains, a lower-level moistening leads to a more organized (stronger) deep convective activity (WS1) just to the west followed by the appearance of the AEW signature in the meridional winds downstream of Ethiopian highlands. This sequence of events (slightly) favors the interpretation that it is the changing of the deep convection from WS3 to WS1 type that transforms a wave on the upper-level TEJ into the lower-level AEW, instead of the convective changes being passive expressions of this transformation.

Future study will examine two seemingly plausible explanations: (i) The WS3-type convection transitions to WS1-type convection between Ethiopian highlands and Darfur mountains and together they force AEW signal downstream, or (ii) the AEW signals appear as a response to increased convective heating over the mountains and ''organizes'' the convective activity into WS1-style activity. Presently, we speculate that the WS3-type transitions into WS1-type and the dynamic response to the increased heating by the more organized and stronger convection initiates the AEW.

Our analysis also examined the nature and possible causes of the westward propagation of the enhanced WS3-type convective activity. Although the mean low-level flow over the western Indian Ocean off the coast of Somalia is predominantly westerly up to about the 600-hPa level, the mean flow over the northern Arabian Sea and Arabian landmass above the 700-hPa level is easterly and reaches a maximum in the upper troposphere. Hence, the westward propagation of the convective activity anomaly appears to be steered by the upper-level mean flow.

The mechanisms that may be associated with convective system development and their propagation over tropical Africa were examined. Increased convection is broadly in phase with the region of low-level moisture flux convergence, indicating an important role of moisture convergence particularly for producing WS1-type systems over eastern Africa. However, a key role of the vertical shear in the winds cannot be excluded as suggested by the association of these events with upper-level wind divergence. The role of upper-level wind divergence seems to be more important for WS1 systems than for the WS3 convection. The upper-tropospheric easterly waves appear to strengthen the enhanced, but scattered, convection (WS3) over the region east of 40°E but also reinforce the more vigorous convection (WS1) to the west of this.

Overall, the results here demonstrate a sequence of events that show enhanced, scattered, and weaker WS3-type activity that starts over the Arabian Sea and western Indian Ocean, propagates westward, and transitions to a more organized and strong WS1-type convection to the west of Ethiopian highlands. The convective transition appears before the AEW signals are seen downstream of the Ethiopian highlands.

This study has revealed interesting results concerning the relationship between various types of convectively active cloud systems and the AEW. Consistent with earlier studies (e.g., MTA06; THK08; Leroux and Hall 2009), our results show that convection over East Africa triggers the AEWs. However, some details are yet to be understood. We still do not know the precise mechanism for the transition from WS3 to WS1 or how WS1 initiates the AEW. Nor do we understand why the magnitude of

the AEW varies. The role of Ethiopian mountains in the transition process is not fully investigated. To investigate these questions requires both a higher space–time-resolution analysis of events over the Ethiopian highlands, especially the role that might be played by the diurnal variations of convection, and modeling studies to elucidate the role of wind shear and other aspects of the dynamical interaction of the deep convection and upper-level and lower-level waves.

Acknowledgments. This research was supported by NASA Grants NNXD7AN04G (Modeling Analysis and Prediction) and NNXD7AT10G (*CloudSat*/CALIPSO). ERA-40 is obtained from the ECMWF data server at www.ecmwf.int. Initial processing of the weather state dataset was done by A. Polak. We benefited from conversations with George Kiladis of NOAA/Boulder, Chris Thorncroft of University at Albany, and Eric Tromeur of the City College of New York. We also thank two anonymous reviewers for their useful comments, which greatly improved the paper.

REFERENCES

Adler, R. F., and Coauthors, 2003: The version 2 Global Precipitation Climatology Project (GPCP) monthly precipitation analysis (1979–Present). *J. Hydrometeor.,* **4,** 1147–1167.

Albignat, J. P., and R. J. Reed, 1980: The origin of African wave disturbances during Phase III of GATE. *Mon. Wea. Rev.,* **108,** 1827–1839.

Anderberg, M. R., 1973: *Cluster Analysis for Applications*. Elsevier, 359 pp.

Avila, L. A., and R. J. Pasch, 1992: Atlantic tropical systems of 1991. *Mon. Wea. Rev.,* **120,** 2688–2696.

Berry, G. J., and C. D. Thorncroft, 2005: Case study of an intense African easterly wave. *Mon. Wea. Rev.,* **120,** 2688–2696.

Burpee, R. W., 1972: The origin and structure of easterly waves in the lower troposphere of North Africa. *J. Atmos. Sci.,* **29,** 77–90.

Cadet, D. L., and N. O. Nnoli, 1987: Water vapour transport over Africa and the Atlantic Ocean during summer 1979. *Quart. J. Roy. Meteor. Soc.,* **113,** 581–602.

Carlson, T. N., 1969a: Synoptic histories of three African disturbances that developed into Atlantic hurricanes. *Mon. Wea. Rev.,* **97,** 256–275.

——, 1969b: Some remarks on African disturbances and their progress over tropical Atlantic. *Mon. Wea. Rev.,* **97,** 716–726.

Charney, J. G., and M. E. Stern, 1962: On the stability of internal baroclinic jets in a rotating atmosphere. *J. Atmos. Sci.,* **19,** 159–172.

Dickinson, M., and J. Molinari, 2000: Climatology of sign reversals of the meridional potential vorticity gradient over Africa and Australia. *Mon. Wea. Rev.,* **128,** 3890–3899.

Duchon, C. E., 1979: Lanczos filtering in one and two dimensions. *J. Appl. Meteor.,* **18,** 1016–1022.

Duvel, J. P., 1989: Convection over tropical Africa and the Atlantic Ocean during northern summer. Part I: Interannual and diurnal variations. *Mon. Wea. Rev.,* **117,** 2782–2799.

——, 1990: Convection over tropical Africa and the Atlantic Ocean during northern summer. Part II: Modulation by easterly waves. *Mon. Wea. Rev.,* **118,** 1855–1868.

Eltahir, E. A., B. Loux, T. K. Yamana, and A. Bomblies, 2004: A see-saw oscillation between the Amazon and Congo basins. *Geophys. Res. Lett.,* **31,** L233201, doi:10.1029/2004GL021160.

Findlater, J., 1969: A major low-level air current near the Indian Ocean during the northern summer. *Quart. J. Roy. Meteor. Soc.,* **95,** 362–380.

Fu, R., A. DelGenio, and W. B. Rossow, 1990: Behavior of deep convective clouds in the tropical Pacific from ISCCP radiances. *J. Climate,* **3,** 1129–1152.

Hall, N. M. J., G. Kiladis, and C. Thorncroft, 2006: Three dimensional structure and dynamics of African easterly waves. Part II: Dynamical modes. *J. Atmos. Sci.,* **63,** 2231–2245.

Holton, J. R., 1992: *An Introduction to Dynamic Meteorology*. 3rd ed. Academic Press, 511 pp.

Hsieh, J.-S., and K. H. Cook, 2005: Generation of African easterly wave disturbances: Relationship to the African easterly jet. *Mon. Wea. Rev.,* **133,** 1311–1327.

Jakob, C., and G. Tselioudis, 2003: Objective identification of cloud regimes in the Tropical Western Pacific. *Geophys. Res. Lett.,* **30,** 2082, doi:10.1029/2003GL018367.

Kiladis, G. N., and M. Wheeler, 1995: Horizontal and vertical structure of observed tropospheric equatorial Rossby waves. *J. Geophys. Res.,* **100,** 22 981–22 997.

——, C. D. Thorncroft, and N. G. Hall, 2006: Three-dimensional structure and dynamics of African easterly waves. Part I: Observations. *J. Atmos. Sci.,* **63,** 2212–2230.

Krishnamurti, T. N., 1971: Observational study of the tropical upper-tropospheric motion field during the Northern Hemispheric summer. *J. Appl. Meteor.,* **10,** 1066–1096.

——, and H. N. Bhalme, 1976: Oscillations of a monsoon system. Part I: Observational aspects. *J. Atmos. Sci.,* **33,** 1937–1954.

Leroux, S., and N. M. J. Hall, 2009: On the relationship between African easterly waves and the African easterly jet. *J. Atmos. Sci.,* **66,** 2303–2316.

——, ——, and G. N. Kiladis, 2009: A climatological study of transient-mean flow interactions over West Africa. *Quart. J. Roy. Meteor. Soc.,* **136,** 397–410.

Levin, N. E., E. J. Zipser, and T. E. Cerling, 2009: Isotopic composition of waters from Ethiopia and Kenya: Insights into moisture sources for eastern Africa. *J. Geophys. Res.,* **114,** D23306, doi:10.1029/2009JD012166.

Lin, Y. L., K. E. Robertson, and C. M. Hill, 2005: Origin and propagation of a disturbance associated with an African easterly wave as a precursor of Hurricane Alberto (2000). *Mon. Wea. Rev.,* **133,** 3276–3298.

Machado, L. A. T., and W. B. Rossow, 1993: Structural characteristics and radiative properties of tropical cloud clusters. *Mon. Wea. Rev.,* **121,** 3234–3260.

——, ——, R. L. Guedes, and A. W. Walker, 1998: Life cycle variations of mesoscale convective systems over the Americas. *Mon. Wea. Rev.,* **126,** 1630–1654.

Mekonnen, A., 2007: Synoptic-scale convection and wave activity over tropical Africa and the Atlantic. Ph.D. thesis, University at Albany, 158 pp.

——, C. D. Thorncroft, and A. Aiyyer, 2006: Analysis of convection and its association with African easterly waves. *J. Climate,* **19,** 5405–5421.

Mishra, S. K., and M. K. Tandon, 1983: A combined barotropic–baroclinic instability study of the upper-tropospheric easterly jet. *J. Atmos. Sci.,* **40,** 2708–2723.

Norquist, C. D., E. E. Recker, and R. J. Reed, 1977: The energetics of African wave disturbances as observed during Phase III of GATE. *Mon. Wea. Rev.,* **105,** 334–342.

Pytharoulis, I., and C. Thorncroft, 1999: The low-level structure of African easterly waves in 1995. *Mon. Wea. Rev.,* **127,** 2266–2280.

Reed, R. J., D. C. Norquist, and E. E. Recker, 1977: The structure and properties of African wave disturbances as observed during Phase III of GATE. *Mon. Wea. Rev.,* **105,** 317–333.

——, E. Klinker, and A. Hollingsworth, 1988: The structure and characteristics of African easterly wave disturbances determined from ECMWF operational analysis/forecast system. *Meteor. Atmos. Phys.,* **38,** 22–33.

Rossow, W. B., and R. A. Schiffer, 1999: Advances in understanding clouds form ISCCP. *Bull. Amer. Meteor. Soc.,* **80,** 2261–2287.

——, G. Tselioudis, A. Polak, and C. Jakob, 2005: Tropical climate described as a distribution of weather states indicated by distinct mesoscale cloud property mixtures. *Geophys. Res. Lett.,* **32,** L21812, doi:10.1029/2005GL024584.

Schiffer, R. A., and W. B. Rossow, 1983: The International Satellite Cloud Climatology Project (ISCCP): The first project of the World Climate Research Programme. *Bull. Amer. Meteor. Soc.,* **64,** 779–784.

Tadesse, T., 1994: The influence of the Arabian Sea storms/depressions over the Ethiopian weather. *Proc. Int. Conf. on Monsoon Variability and Prediction,* Geneva, Switzerland, World Meteorological Organization, 228–236.

Thorncroft, C. D., and B. Hoskins, 1994a: An idealized study of African easterly waves. I: A linear view. *Quart. J. Roy. Meteor. Soc.,* **120,** 953–982.

——, and ——, 1994b: An idealized study of African easterly waves. II: A nonlinear view. *Quart. J. Roy. Meteor. Soc.,* **120,** 983–1015.

——, and K. Hodges, 2001: African easterly wave variability and its relationship to Atlantic Ocean tropical cyclone activity. *J. Climate,* **14,** 1166–1179.

——, N. M. J. Hall, and G. N. Kiladis, 2008: Three-dimensional structure and dynamics of African easterly waves. Part III: Genesis. *J. Atmos. Sci.,* **65,** 3596–3607.

Tromeur, E., and W. B. Rossow, 2010: Interaction of tropical deep convection with the large-scale ciculation in MJO. *J. Climate,* **23,** 1837–1853.

Washington, R., and Coauthors, 2006: African climate change: Taking a shorter route. *Bull. Amer. Meteor. Soc.,* **87,** 1355–1366.

Wheeler, M., and G. N. Kiladis, 1999: Convectively coupled equatorial waves: Analysis of clouds and temperature in the wavenumber–frequency domain. *J. Atmos. Sci.,* **56,** 374–399.

——, ——, and P. J. Webster, 2000: Large-scale dynamical fields associated with convectively coupled equatorial waves. *J. Atmos. Sci.,* **57,** 613–640.

Zhang, Y., W. B. Rossow, A. A. Lacis, V. Oinas, and M. I. Mishchenko, 2004: Calculation of radiative fluxes from the surface to top of the atmosphere based on ISCCP and other global data sets: Refinements of the radiative transfer model and the input data. *J. Geophys. Res.,* **109,** D19105, doi:10.1029/2003JD004457.